



Modeling the 2012 May 17 Solar Energetic Particle Event Using the AWSoM and iPATH Models

Gang Li¹, Meng Jin², Zheyi Ding^{1,3}, A. Bruno^{4,5}, G. A. de Nolfo⁴, B. M. Randol⁴, L. Mays⁶, J. Ryan⁷, and D. Lario⁴

¹ Department of Space Science and CSPAR, University of Alabama in Huntsville, Huntsville, AL 35899, USA; gang.li@uah.edu

² Lockheed Martin Solar & Astrophysics Laboratory, USA

³ School of Geophysics and Information Technology, China University of Geosciences (Beijing), Beijing 100083, People's Republic of China

⁴ Heliophysics Division, NASA Goddard Space Flight Center, Greenbelt, MD, USA

⁵ Department of Physics, Catholic University of America, Washington, DC, USA

⁶ CCMC, NASA Goddard Space Flight Center, Greenbelt, MD, USA

⁷ Physics Department, University of New Hampshire, Durham, NH, USA

Received 2021 April 25; revised 2021 June 18; accepted 2021 June 21; published 2021 October 5

Abstract

We model the 2012 May 17 solar energetic particle event by combining the AWSoM and iPATH codes. Using this combined approach, we investigate particle acceleration when the parent coronal mass ejection (CME) is still close to the Sun. We have obtained reasonable agreements between our simulation and observations made by multiple spacecraft. We follow the three-dimensional CME and the CME-driven shock from their initiation using the AWSoM code for a period of 3 hours when the shock is below $\sim 20 R_s$. Above $20 R_s$, iPATH2D is used to follow the CME-driven shock. The plasma properties from the AWSoM code are fed into the iPATH model, where particle acceleration at the shock front is modelled and the instantaneous energetic particle spectra are obtained. The subsequent transport of these energetic particles in the solar wind is followed using the iPATH model. We obtain both the instantaneous particle spectra and particle fluence at 1 au, and we then compare them with observations. To account for uncertainties of magnetic field connectivity from 1 au to the shock, as well as uncertainties of the shock profiles, our model's results are obtained as an ensemble average where, instead of considering Earth as a single point location, we consider multiple locations within 10 degrees in longitude and latitude from Earth. The effect of this model uncertainty mimics that of the field line meandering, as suggested by Bian & Li, but is of different origin. We suggest that a trustworthy solar energetic particle forecast should be made in an ensemble average approach.

Unified Astronomy Thesaurus concepts: Solar energetic particles (1491)

1. Introduction

Coronal mass ejections (CMEs) constitute a major space weather concern. In large CMEs, considerable coronal material can be ejected with energies reaching 10^{31-32} ergs. The fast moving ejected coronal material can produce shock waves in front of the CME. These shocks can accelerate ions to several GeV per nucleon (see, e.g., Mewaldt et al. 2005; Mewaldt 2006) and consequently CME-driven shocks are often regarded as the major sites for acceleration of Solar Energetic Particles (SEPs).

The main particle acceleration process at CME-driven shocks is believed to be diffusive shock acceleration (DSA), which is also known as first-order Fermi acceleration. DSA was proposed to explain the acceleration of galactic cosmic rays in supernova shocks by Axford et al. (1977); Krymskii (1977); Blandford & Ostriker (1978); Bell (1978a, 1978b). An earlier attempt to apply the DSA to interplanetary shocks by Lee (1983) solved the coupled particle transport and upstream Alfvén wave intensity equations. The work of Lee (1983) was extended by Gordon et al. (1999) and Lee (2005). In the work of Gordon et al. (1999), the authors compared the steady-state solutions of energetic particles and the upstream wave spectra with observations at the Earth's bow shock. The steady-state solutions by Gordon et al. (1999) was appropriate because the bow shock is stationary. However, for a propagating CME-driven shock, the shock parameters and the solar wind plasma vary with the heliocentric distance. Consequently, the problem of particle acceleration in SEP events is intrinsically time-dependent and thus more

difficult. It is worth noting that shock acceleration has also been invoked to explain flare-accelerated SEPs that escape to the interplanetary medium (in comparison to those precipitate down to solar surface) by Lee & Ryan (1986).

The origin of the low-energy SEPs has been deduced by observations of their morphology and composition. SEP events generally, though not exclusively, fall into two categories: impulsive and gradual SEPs. Impulsive events are generally small, electron rich, and tend to be enriched in heavy ions with $^3\text{He}/^4\text{He} \sim 1$. Gradual events tend to be large, last much longer than impulsive events, and have elemental abundances and charge states that are representative of solar coronal material and temperatures (i.e., 10^6 K). Many models have been developed to explain SEPs. In the work of Ng et al. (2003), the same set of equations as Lee (1983, 2005) were solved with a simple shock profile where the shock speed and the Alfvén Mach number are predefined. These authors showed that the upstream proton-enhanced waves can be greatly enhanced from the quiet background solar wind value. In another work, Zank et al. (2000) took a different approach in dealing with the time dependence of the wave amplification. Zank et al. (2000) adopted the steady-state DSA solution at a series of times, but constrained the maximum particle energy at these times by balancing the shock dynamic timescale with the particle acceleration timescale. Using the ZEUS MHD code, Zank et al. (2000) numerically followed the propagation of a CME-driven shock. In this formalism, the coupled Parker transport

equation and the wave action transport equation are solved at the shock front. Accelerated particles are followed in an onion-shell model behind the shock and those that escape upstream of the shock are followed assuming a ballistic propagation. This work has been further extended by Rice et al. (2003); Li et al. (2003, 2005) and was the foundation of the Particle Acceleration and Transport (PATH) model.

The works by Rice et al. (2003) and Li et al. (2003, 2005) considered only 1D shocks. However, it has been shown by Li et al. (2009, 2012b) that the shock geometry can have a critical role in regulating the acceleration process and can determine (for example) the Q/A -dependence of the spectral break locations, which is a spectral feature that is often observed in gradual SEP events (Mewaldt et al. 2005). Hu et al. (2017) have extended the PATH model to a 2D geometry, leading to the iPATH 2D model. Compared to the original PATH code, iPATH relies on a 2D ZEUS MHD code to provide the background solar wind and the CME-driven shock and includes particle perpendicular diffusion in the transport module. Using the iPATH model, Hu et al. (2018) examined how the nature of a single SEP event varies with longitude and heliocentric distance. Additionally, Fu et al. (2019) also examined how the event fluence can vary as a function of the solar rotation rate.

In the past decade, the 1D PATH model has been used to simulate individual SEP events with moderate success. For example, the 2001 September 29 event was examined by Verkhoglyadova et al. (2009) and the 2006 December 13 event by Verkhoglyadova et al. (2010). A common finding from these event studies is that the iPATH model can reproduce the time intensity profiles of low-energy protons quite well—see, for example, Figures 3 and 4 in Verkhoglyadova et al. (2009) and Figure 4 in Verkhoglyadova et al. (2010)—but the simulations seem to predict a deficit of high-energy protons and ions—see, for example, Figure 2 in Verkhoglyadova et al. (2009) and Figure 8(a) in Verkhoglyadova et al. (2010). The agreement in low-energy ($< \sim 100$ MeV) particles but deficit at high-energy ($> \sim 100$ MeV) particles between the observation and the PATH model results reveals two things. First, the acceleration of low-energy particles must occur during an extended period with a significant portion of them accelerated when the CME-driven shock is beyond $10 R_s$. The acceleration of these particles must also occur in an extended region so that even the 1D PATH model is capable of describing the characteristics of these particles. Second, and more importantly, the acceleration of high-energy particles likely occurs well below $10 R_s$, and is therefore outside the simulation domain of the PATH and the iPATH model.

Observations of Type II radio bursts suggest that shocks can form at heights below $2 R_s$ and estimates of the release times of the first high-energy particles observed in this and other SEP events suggest that those particles may be released from the shock soon after its formation (Gopalswamy et al. 2013). Such a low release height of energetic protons and ions is common for Ground Level Enhancement events (Reames 2009a, 2009b). The particle release heights for large gradual SEP events are somewhat higher than GLE events but, even for events generated by filament eruptions where no conspicuous flare is observed, the release heights for SEPs can still be below $10 R_s$ (Gopalswamy et al. 2017). These observations highlight the necessity of simulating particle acceleration at CME-driven shocks close to the Sun. Additionally, the energy spectra measured in SEP events from low (\sim keV) to high (\sim GeV) energies indicate the need to

consider both acceleration and transport effects from the early formation of the shocks. Many gradual SEP events exhibit spectral features that indicate important transitions between acceleration and transport processes. High-energy observations from the Payload for Antimatter Matter Exploration and Light-nuclei Astrophysics (PAMELA) mission have established that there is a universal spectral roll-over (Bruno et al. 2018, 2019) that is distinct from the well-studied spectral break at low energies (Li et al. 2009; Desai et al. 2016). Together, these observations demonstrate the need to model particle acceleration, particularly at high energy, by taking into account the properties of the CME-driven shock early in its development, well below $10 R_s$.

To examine the shock profile close to the Sun, one needs a sophisticated CME model that can capture the initiation and evolution of the CME, as well as the shock that it drives. In the work of Kozarev et al. (2013), an earlier version of the Alfvén Wave Solar Model (AWSoM; van der Holst et al. 2010; Manchester et al. 2012), that modeled the initiation and propagation of CMEs, was combined with the Earth Moon Mars Radiation Environment Module (EMMREM) (Schwadron et al. 2010), which is a solver of the focused particle transport equation, to model the acceleration of particles by a CME-driven shock below $8 R_s$.

The AWSoM code uses analytical magnetic flux ropes to initiate CMEs. Because the presence of the magnetic flux is essential for the CME initiation, the AWSoM code can achieve a more realistic description of a CME and the shock than the ZEUS code. However, the EMMREM code that is used in Kozarev et al. (2013) does not solve the wave transport equation explicitly, and an ad-hoc assumption of the particle diffusion coefficient has to be made in modelling the accelerated particle spectra. In a recent attempt, Linker et al. (2019) combined the Corona-Heliosphere (CORHEL) code with EMMREM and applied it to the 2000 July 14 event. The combined Solar particle event Threat Assessment Tool (STAT) developed by Linker et al. (2019) provides users with many useful diagnostic for understanding gradual SEP events from a space weather perspective. Nevertheless, the aforementioned ad-hoc assumption of the diffusion coefficient in EMMREM can greatly affect the resulting particle spectra, especially at the high energy end.

In this work, we combine the AWSoM model with the iPATH model to study the 2012 May 17 event. We use the AWSoM code to model the CME initiation and the shock that it drives for the first 3 hr, when the CME-driven shock is below $20 R_s$. Plasma parameters from the AWSoM code are fed into the iPATH code in which the accelerated particle spectra at the shock is computed and the transport of energetic particles in the heliosphere is followed. After 3 hr and beyond $20 R_s$, we use only the iPATH model to follow the CME-driven shock because following a CME and the shock that it drives using the AWSoM code beyond $20 R_s$ is computationally demanding. Furthermore, as we discussed earlier, the PATH and iPATH model capture the characteristics of low-energy particles well (Verkhoglyadova et al. 2009, 2010) so that we use the AWSoM code to focus only on the acceleration of high-energy particles. The combination of AWSoM+iPATH provides both (1) a realistic description of the shock below $20 R_s$ (similar to the works by Kozarev et al. 2013; Borovikov et al. 2018; Linker et al. 2019), and (2) a physics-based description of the particle diffusion coefficient at the shock front through the iPATH model. Therefore, we address the

problem of particle acceleration and transport in a self-consistent manner by considering the properties of the CME-driven shock close to the Sun.

The 2012 May 17 event has been the subject of many analyses in the literature. The work by Gopalswamy et al. (2013) examined the eruption sequence and deduced the energetic particle release heights. Shen et al. (2013) examined the pre-event magnetic field configuration and suggested that the eruption contains two episodes within 2 minutes. Such a compound eruption can be favorable for particle energization (Li et al. 2012a). Li et al. (2013) compared the release times of electrons and ions, and found that energetic electrons were released earlier than energetic ions, and were more likely to be due to the flare while energetic ions were associated with the CME-driven shock. Later analyses by Firoz et al. (2014) and Ding et al. (2016) tended to support this conclusion. However, energetic electrons were observed by STEREO in Dresing et al. (2014), indicating a significant longitudinal spreading of energetic electrons, which can be the result of either a meandering interplanetary magnetic field (IMF) or the energization (or re-energization) at a spatially extended shock. While there were many observational reports about this event, modeling attempts were lacking. Recently, Battarbee et al. (2018) examined the transport of sub-GeV protons in this event using a 3D transport code. They compared their model results with observations at multiple locations made by Geostationary Operational Environmental Satellites (GOES), SOHO/ERNE, STEREO-A/B, MSL/RAD, and MESSENGER. By fitting the time profiles at multiple spacecraft, they found that high-energy particles are injected into the IMF near the flare location, which indicates that the acceleration is also more efficient near the flare region. This is consistent with the scenario of acceleration of high-energy particles at a CME-driven shock with a height lower than $10 R_s$. The work of Battarbee et al. (2018) put constraints on the underlying acceleration process by decoupling the transport process from the acceleration process. Here, we explicitly consider the acceleration process at the shock which varies as the shock evolves. As in Battarbee et al. (2018), we also consider the transport of energetic particles using a 3D code. To our knowledge, our modeling effort is the first to combine the following three important ingredients of SEP modeling into a single numerical simulation: (1) follow a CME eruption and its propagation from the solar surface, (2) consider particle acceleration at the CME-driven shock with a physics description of the particle diffusion coefficient, and (3) include particle transport in the IMF.

Our paper is organized as follows. In Section 2, we briefly discuss the AWSoM and iPATH models. Section 2.1 discusses the AWSoM model. Instead of discussing the details of the model, we focus on how to extract plasma and shock information from the AWSoM that will be fed into the iPATH model. Section 2.2 discusses the iPATH model, where we focus on how we incorporate the various shock and solar wind parameters from the AWSoM code into the iPATH code. Section 3 compares our simulation results and the observations. The main conclusions of this work are summarized in Section 4.

2. Model Setup

2.1. AWSoM Solar Wind and CME Model

The AWSoM (van der Holst et al. 2014; Sokolov et al. 2013) model was developed under the Space Weather Modeling

Framework (Tóth et al. 2012) at the University of Michigan. The AWSoM simulation domain starts from the solar upper chromosphere, and extends into the corona and heliosphere. A steady-state solar wind solution is obtained with the local time stepping and second-order shock-capturing scheme. The inner boundary condition of the magnetic field is specified by GONG synoptic magnetograms. The inner boundary conditions for electron and proton temperatures T_e and T_i and number density n are assumed at $T_e = T_i = 50,000$ K and $n = 2 \times 10^{17} \text{ m}^{-3}$, respectively. The initial conditions for the solar wind plasma are specified by the Parker solution (Parker 1958), while the initial magnetic field is based on the Potential Field Source Surface (PFSS) model with the Finite Difference Iterative Potential Solver (FDIPS, Tóth et al. 2011). Alfvén waves are driven at the inner boundary with a Poynting flux that scales with the surface magnetic field. Electron heat conduction (both collisional and collisionless) and radiative cooling are also included in the model. By using a physically consistent treatment of wave reflection, dissipation, and heat partitioning between the electrons and protons, AWSoM has demonstrated the capability to reproduce a high-fidelity solar corona environment (van der Holst et al. 2014; Jin et al. 2017a).

In this study, we initiate the CME using the analytical Gibson-Low (GL; Gibson & Low 1998) flux rope. Analytical profiles of the GL flux rope are obtained by finding a solution to the magnetohydrostatic equation $(\nabla \times \mathbf{B}) \times \mathbf{B} - \nabla p - \rho \mathbf{g} = 0$ and the solenoidal condition $\nabla \cdot \mathbf{B} = 0$. This solution is derived by applying a mathematical stretching transformation $r \rightarrow r - a$ to an axisymmetric, spherical ball of twisted magnetic flux. To determine the GL flux rope parameters, we use the Eruptive Event Generator Gibson-Low (EEGGL; Jin et al. 2017b) module that was recently developed to calculate GL flux rope parameters through a handful of observational quantities, so that the modeled CMEs can propagate with the desired CME speeds near the Sun. The GL flux rope and contained plasma are then superposed onto the steady-state solar corona solution; that is, $\rho = \rho_0 + \rho_{\text{GL}}$, $\mathbf{B} = \mathbf{B}_0 + \mathbf{B}_{\text{GL}}$, $p = p_0 + p_{\text{GL}}$. The combined background-flux rope system is in a state of force imbalance and erupts immediately after the simulation is advanced forward in time. For the specific event analyzed here, we run the simulation for 6 hr after CME onset, when the CME has passed $30 R_s$ into the heliosphere.

At the first time step, the shock is obtained as a 2D surface (i.e., mathematically, r as a function of θ and ϕ). Each point on the shock surface given by (θ, ϕ, r) is associated with a data structure containing the shock compression ratio, obliquity angle θ_{BN} , shock Mach number M_{sh} , and shock speed V_{sh} at that location. For details of how the shock locations are determined and the shock parameters are calculated, we refer the reader to Section 3 and Jin et al. (2018). We first use the proton temperature gradient as the criteria to determine whether a shock exists in certain region and we set 0.03 of the maximum gradient in the domain as a threshold. The entropy criteria is then used to determine the up- and downstream locations, and the shock parameters will be calculated. Based on this calculation, part of the initial shock locations could be rejected if the compression ratio is less than unity. We further record the solar wind velocity at the numerical grid point that has the same θ and ϕ but a smaller r_g with $r - r_g < \Delta r$. Here, Δr is the numerical grid along r in the AWSoM model. At the second time step, the newer shock locations are obtained in a similar fashion. Furthermore, the first shell that contains

multiple cells (corresponding to different θ 's and ϕ 's) is obtained as follows: the outer boundary of this shell corresponds to the current shock location, and the inner boundary is obtained by advecting the grid points (with r_g 's) that are behind the shock in the first time step. The plasma in those locations will propagate out to their new locations with their corresponding plasma velocities saved at the first time. These new locations are then meshed to the 2D (θ, ϕ) space in the simulation domain to yield the inner boundary of the first shell. Particles accelerated between the first time step and the second time step will populate into this shell. At later times, old shells will advect out and a new shell will be created behind the shock in the same fashion as in the second time step. The plasma parameters of all shells are saved in the data structure that is associated with this time, and are used to obtain the new locations of these shells in the next time step.

2.2. iPATH Particle Acceleration and Transport Model

We revise the iPATH 2D model (Hu et al. 2017, 2018) by extending it to take plasma inputs from the AWSoM code. The iPATH model consists of three modules. The first module of iPATH is based on the ZEUS 2D MHD code that simulates the background solar wind and the CME-driven shock by perturbing the inner boundary of the simulation domain, which is often set at 20 or 10 R_s . In this work, this module is replaced by the AWSoM model, as explained in Section 2.1. The second module of iPATH computes the accelerated particle spectra at the shock front, assuming that the acceleration mechanism is DSA. Accelerated particles can convect with the shock downstream of the shock. This convection is followed using a 2D shell model in the iPATH code, and is revised here to a 3D cell model (see below). Once particles diffuse far enough upstream of the shock, they can escape from the shock complex. The third module of iPATH follows the propagation of these particles in the solar wind, along and across the background interplanetary magnetic field, using a backward stochastic differential equation method.

Note that in the second module, at every time step the instantaneous particle spectrum is obtained by only using the shock parameters at that time. These newly accelerated particles are distributed only in the first shell behind the shock. The diffusion of particles among the first shell and all other shells constructed earlier must be followed. Therefore, all of the shells that were constructed earlier have to be identified and tracked in the AWSoM code, as discussed in 2.1. In contrast to the work by Hu et al. (2017) and Hu et al. (2018), where the shock was given by a curve since only the ecliptic plane was considered, the shock structure from the 3D AWSoM code is a 2D surface. Therefore, when we consider particle diffusion among parcels and escaping upstream of the shock, we need to consider a 2D mesh identified by (θ, ϕ) instead of just a 1D segment identified by ϕ only. Modifying the 2D parcel structures in the iPATH model to a 3D cell structure marks the major revision of the iPATH 2D code in this work. This is achieved by adding a wrapper code that serves as an interface to pass all of the plasma parameters at the shock front and in the individual cells behind the shock from AWSoM to iPATH.

Following Ding et al. (2020), the instantaneous particle distribution function at the shock front is assumed to be of a

power law multiplied by an exponential decay,

$$f(\mathbf{r}, p, t_k) = c_1^* \epsilon_r n_{t_k, \mathbf{r}} p^{-\beta} H[p - p_{\text{inj}, \mathbf{r}}] \exp\left(-\frac{E}{E_{0, \mathbf{r}}}\right) \quad (1)$$

where $\beta = 3s_r/s_r - 1$, s_r is the shock compression ratio at \mathbf{r} , ϵ_r is the injection efficiency, $n_{t_k, \mathbf{r}}$ is the upstream solar wind density, $p_{\text{inj}, \mathbf{r}}$ is the particle injection momentum, and $E_{0, \mathbf{r}}$ is the kinetic energy that corresponds to a cutoff momentum $p_{\text{max}, \mathbf{r}}$, which is obtained by balancing the shock dynamic timescale t_{dyn} with the particle acceleration timescale (Drury 1983; Zank et al. 2000):

$$t_{\text{dyn}} = \int_{p_{\text{inj}, \mathbf{r}}}^{p_{\text{max}, \mathbf{r}}} \frac{3s_r}{s_r - 1} \frac{\kappa_r}{U_r^2} \frac{1}{p} dp, \quad (2)$$

where $p_{\text{inj}, \mathbf{r}}$ is the injection momentum, κ_r is the particle diffusion coefficient, U_r is the upstream solar wind speed in the shock frame. Note that all these parameters are functions of \mathbf{r} and vary along the shock surface. Furthermore, κ_r also depends on momentum p . They are calculated at the shock front using plasma and shock parameters determined from the AWSoM module. Note that the shock acceleration process is intrinsically a statistical process, therefore a sudden cutoff in momentum is nonphysical because, for a given amount of time, particles starting from the same initial momentum can reach a range of different momenta (Drury 1983), although the probability of reaching momenta that are beyond $p_{\text{max}, \mathbf{r}}$ decreases quickly. The exponential decay form $\exp(-E/E_0)$ has been adopted from the early work of Ellison & Ramaty (1984). In Equation (1), H is the Heaviside function and c_1 is a normalization constant,

$$c_1 = 1 / \int_{p_{\text{inj}, \mathbf{r}}}^{+\infty} p^{-\beta} e^{-E/E_{0, \mathbf{r}}} d^3p \approx 1 / \int_{p_{\text{inj}, \mathbf{r}}}^{p_{\text{max}, \mathbf{r}}} p^{-\beta} d^3p \quad (3)$$

Downstream of the shock, accelerated particles convect with the shock and diffuse among different cells. Particles can also diffuse out of the shock complex from all cells. We closely follow Ding et al. (2020) in describing the particles' convection and diffusion. Once the particles escape from the shock complex, they propagate along the IMF in the relatively undisturbed solar wind. Their propagation is described by the focused transport equation where the particle pitch angle experiences magnetic focusing and diffusion. Since the unperturbed solar wind magnetic field does not differ much from the Parker field, for simplicity we approximate the upstream solar wind magnetic field by a Parker field in the transport module. The particle flux at a given location \mathbf{r} and a given time t is obtained using the backward stochastic differential equation method (Hu et al. 2017). Note that the cross-field diffusion is easily included in this approach. However, as we explain below, the effect of cross-field diffusion can be ignored by introducing the concept of ensemble simulation, where instead of assuming that an observer is located at a single point, we consider the observer to be located uniformly within a small angular region $\sim 5^\circ$ to 10° . When an observer is magnetically connected to the shock front for an extended period during the shock propagation, including the perpendicular diffusion in an ensemble simulation approach does not change the result.

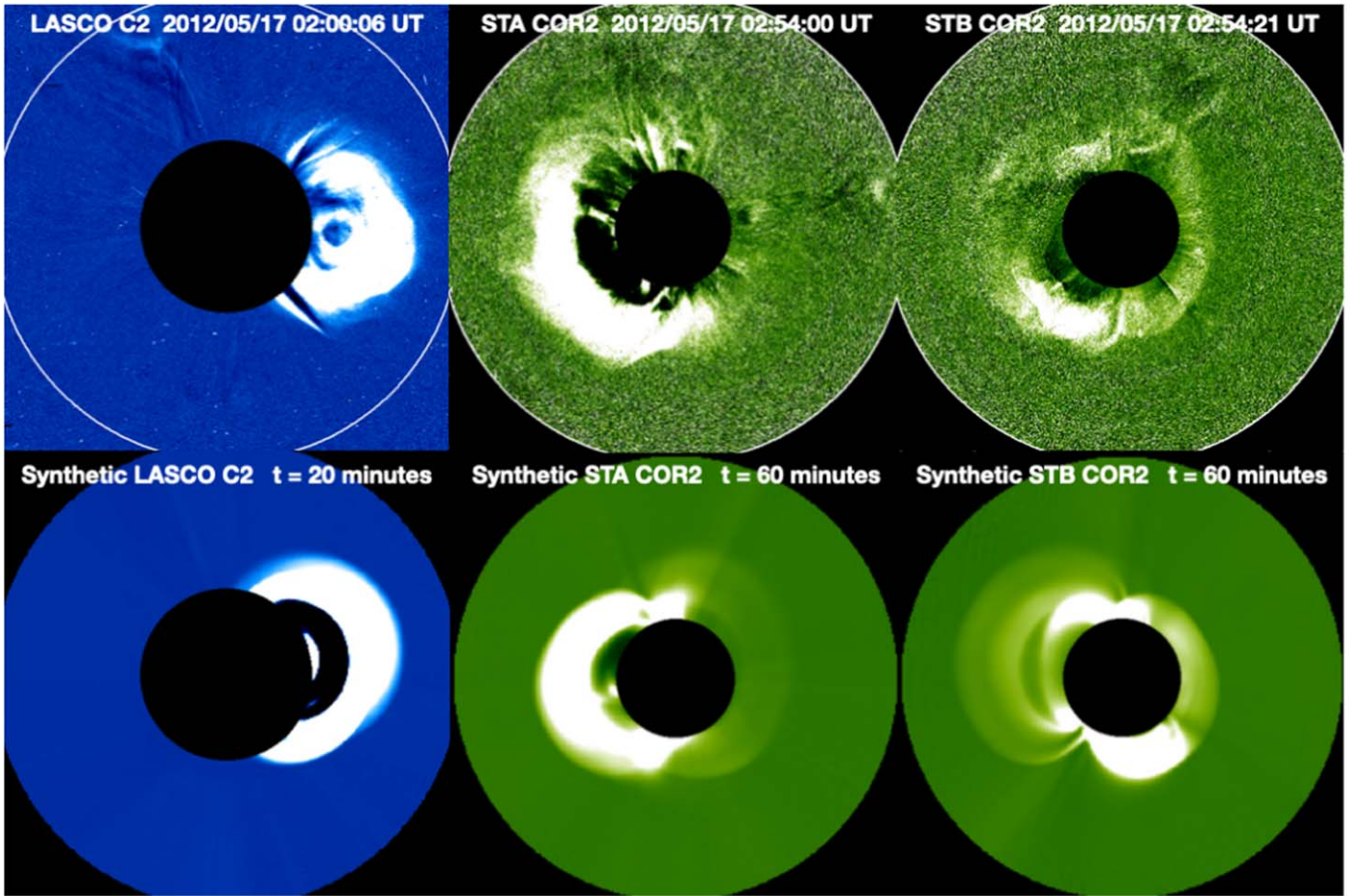


Figure 1. Comparison between the observed white-light images of the 2012 May 17 event from LASCO/C2, STEREO-A/COR2, and STEREO-B/COR2 (shown in the upper panels), to synthetic images from the modeling (shown in the lower panels).

3. Results

An M5 class X-ray flare at 01:25 UT on 2012 May 17 from NOAA active region 11,476 located at N11W76 from Earth’s view point and a fast CME (plane-of-sky speed $\sim 1582 \text{ km s}^{-1}$ according to the CDAW LASCO catalog at cdaw.gsfc.nasa.gov/CME_list/) were associated with the origin of the first GLE event of solar cycle 24 (Gopalswamy et al. 2013). Shen et al. (2013) reported two eruptions that occurred very close in time (within ~ 2 minutes) with the event. For an MHD code to capture such a compound eruption that has only a time separation of ~ 2 minutes is out of the scope of this work. Here we consider only a single eruption and we use white-light observations to fine tune the eruption process.

The near-Sun CME evolution is mainly captured by the white-light observations. We therefore generate synthetic white-light images from the simulation and compare them with the observations from LASCO C2, STA COR2, and STB COR2 (shown from left to right in Figure 1). Note that this event was also associated with global EUV wave (Nitta et al. 2013), rendering another comparison with our MHD simulations, which we do not pursue here. At the time of observation, the separation angles between Earth and STA/B are $\sim 115^\circ$ and $\sim 118^\circ$. Both observation and synthetic images in Figure 1 are produced by subtracting pre-event backgrounds. Note that we do not intend to compare the absolute brightness here, which needs advanced calibration of the observational data and also the inclusion of the contribution from the F corona (e.g.,

Manchester et al. 2008; Jin et al. 2017a). The comparison shows that both the direction of propagation and width of the CME are well reproduced from the three different viewing points.

Figure 2 shows, from left to right, the simulated radial velocity, proton temperature, and magnetic field strength (with projected field lines overlaid) at $t = 30$ minutes after the CME initiation for the $Z = 0$ slice in the heliographic rotating coordinates (i.e., Carrington coordinates). We can clearly see that due to a coronal helmet streamer structure above the CME source region, the CME-driven shock is separated into two distinct structures. Due to differences in the background solar wind speed, one structure is moving faster than the other.

Using the same method as Jin et al. (2018), we derive the 3D shock morphology and parameters at $t = 60$ minutes, as shown in Figure 3. The four panels are for four different shock parameters, which are the compression ratio, the shock speed, the shock Alfvén Mach number, and the angle θ_{Bn} between the upstream magnetic field and the shock normal. Also shown in the figure are field lines that connect to the Earth, STA, and STB, respectively. As we can see from the figure, at this time the earth is connected to a region with a large compression ratio, which implies a more efficient particle acceleration. In comparison, STA is connected to a region with a smaller compression ratio. The field line connecting to STB does not intersect with the shock. Indeed, STB did not intersect with the shock in the entire simulation. Note that for the two distinct

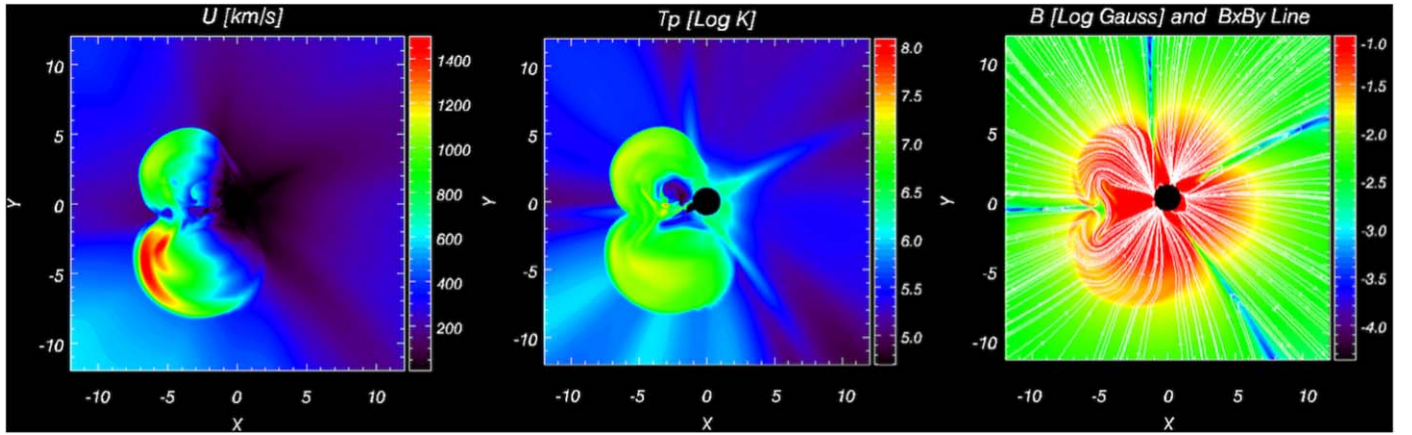


Figure 2. $Z = 0$ slices in the Carrington coordinates of the AWM MHD solution showing the radial velocity, proton temperature, and magnetic field strength (with projected field lines overlaid) at $t = 30$ minutes after the CME initiation.

shock surfaces, the one moving faster (at the left-hand of the Figure connecting to STA) results in a weaker shock (as shown by the smaller compression ratio and Mach number), which demonstrates the importance of considering the inhomogeneous background solar wind where shocks propagate.

The observed particle time profile and spectra at each spacecraft depends on the magnetic connection. For the same event, a spacecraft can detect a large SEP event if it is magnetically connected to a portion of the shock that is favorable for particle acceleration for a longer period of time. In contrast, another spacecraft may only observe a small SEP event if it is connected to a region that is inefficient in particle acceleration. Uncertainties in the magnetic field connection (which are associated with variations in the solar wind velocity) and the cross-field diffusion effects in the transport of energetic particles affect the actual observations of SEPs by a given spacecraft. The presence of cross-field diffusion implies that particles accelerated at the shock, when propagating to 1 au, will have an angular spreading from the original magnetic field lines that the particles tie to (Hu et al. 2017). Conversely, it also means that energetic particles that are observed at a particular location (e.g., L1 point) may originate from multiple locations along the shock surface. This angular spreading of energetic particles depends on particle energy and the shock history. As shown in Hu et al. (2017), a typical choice of $\kappa_{\perp}/\kappa_{\parallel} = 0.01$ leads to a $\sim 10^\circ$ angular spreading of energetic particles at 1 au. Besides cross-field diffusion, model uncertainty can also affect the magnetic connectivity. For example, the intrinsic uncertainty in modeling the solar wind plasma and the CME itself can both affect this magnetic connectivity. For our purpose, such a model uncertainty can be described as an uncertainty of the observer location, i.e., instead of treating Earth as a single point location, we should allow Earth to be within a small region due to model uncertainty. Clearly, both cross-field diffusion and model uncertainty can affect the magnetic connection and lead to an effective stochastic angular spreading of the observer.

This stochastic angular spreading of the observer motivates us to introduce the concept of ensemble modeling. Here what we mean by an ensemble modeling of a SEP event at a particular location is the collection of model results by allowing the location of a spacecraft to vary from a specific point in space within a circle of a given width. By way of example, we consider the angular size of the circle to be 10° in this work,

which is comparable to the angular spreading due to cross-field diffusion as obtained in Hu et al. (2017). Within this angular spreading, we uniformly sample N observer locations and obtain the resulting time profiles and particle spectra by averaging the results from these N simulations. An advantage of using the ensemble modeling approach is that by having N different simulations, one can assess the uncertainty and sensitivity of the model results. This can be particularly attractive and valuable for a forecasting model. Indeed, the variance of this ensemble simulation can be regarded as an approximation of the confidence level. If we consider the circle to have an angular spreading similar to that due to the cross-field diffusion, as we do in this work, then, as a first approximation, one can ignore the cross-field diffusion in the ensemble simulation approach. This approximation has an added numerical advantage, especially when the field line is not described by a well-defined functional form, such as the Parker field. This happens because including cross-field diffusion for an arbitrary field configuration requires us to know not only the magnetic field line along which the particles propagate but also multiple neighboring field lines. This often brings a lot of extra computational slow-downs.

The upper two panels of Figure 4 shows the magnetic connection from Earth and its neighborhood within a 10° circle, to the shock surface at $t = 48$ minutes. A total of 65 field lines were chosen. Because the angular resolution is 1° , some of them trace back to the same point, leading to 52 distinct intersection points at the shock. The size and color of these data points indicate the compression ratio and shock obliquity angle at the shock front at $t = 48$ minutes. As can be seen, these field lines intersect different regions of the shock surface, with different compression ratios and shock obliquity. These differences in the compression ratio will translate into different source spectra at the shock, which emphasizes the role of an ensemble simulation. The choice of 65 field lines is somewhat arbitrary. We have tested both the case of 23 and 65 field lines. The resulting particle spectra and time intensity profiles in both cases are similar, while those for the 65 field lines tend to be slightly smoother. We conclude that a choice of > 50 field lines will be sufficient in the ensemble simulation approach for this event. Note that this number might change for a different event depending on the shock connectivity and the gradient of the shock parameters in that region. The lower two panels of Figure 4 plot show how the shock compression ratio and the

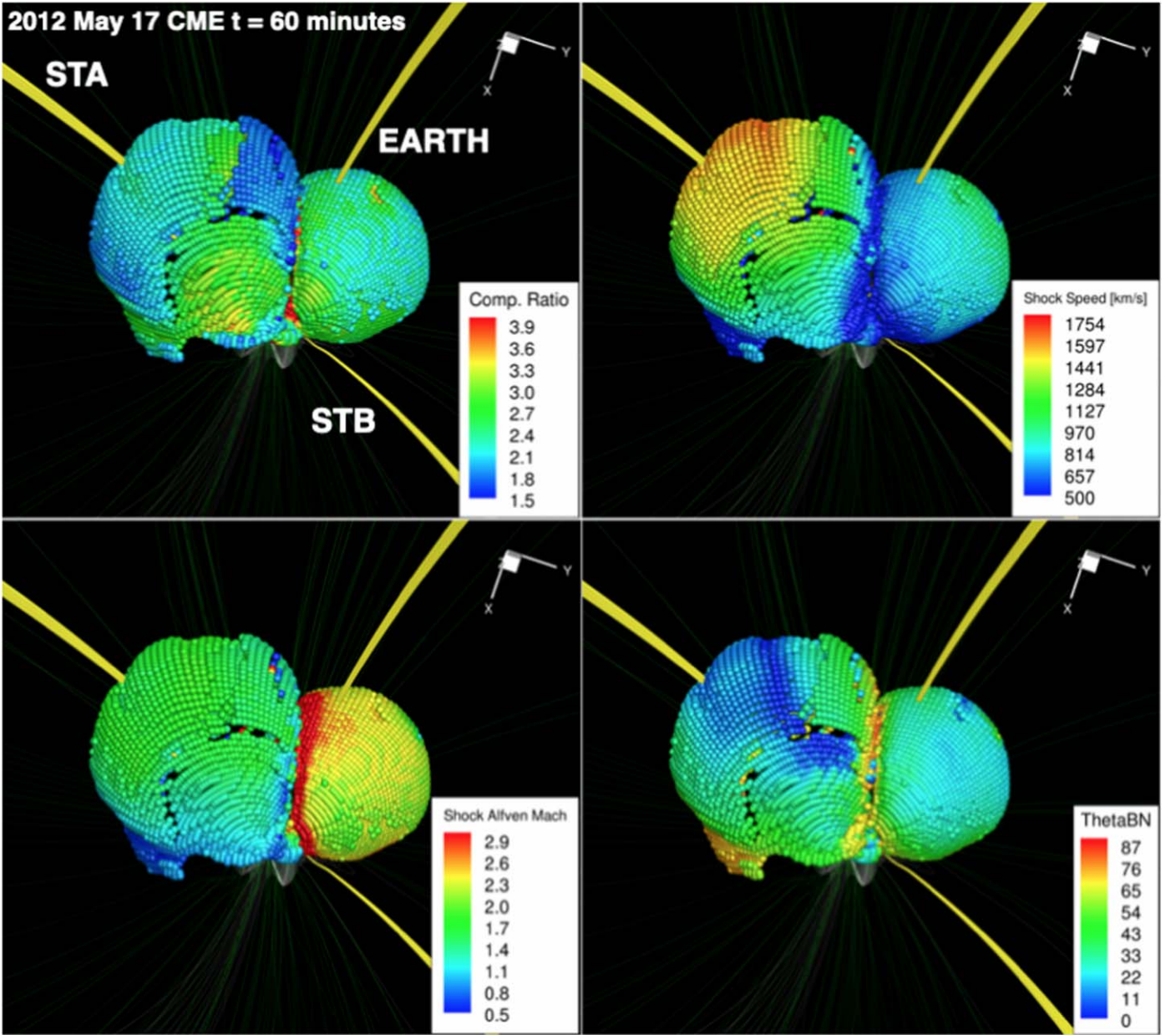


Figure 3. CME-driven shock surface showing the shock compression ratio, shock speed, shock Alfvén Mach number, and shock θ_{Bn} at $t = 60$ minutes. The yellow lines are magnetic field lines that connect to the Earth, STB, and STA, respectively.

shock obliquity angle vary for the first three hours for five random chosen field lines. For all five field lines, the compression ratios drop with time. However, the variation among them is noticeable. For example, at $t = 1$ hr, the maximum compression ratio of these five field lines is 2.25 and the smallest is 1.65, which correspond to spectra $\sim p^{-5.4}$ and $\sim p^{-7.6}$, respectively. Due to the presence of solar wind turbulence, the field line connecting to Earth is unlikely to remain unchanged. Consequently, using an ensemble approach better represents the reality.

As explained earlier, and as practiced in Hu et al. (2017, 2018) and Ding et al. (2020), introducing cross-field diffusion also implies that particles observed at 1 au originate from different regions of the shock. However, unlike considering the cross field alone, the ensemble simulation approach takes into account the intrinsic uncertainties of the modeled observer location that are due to uncertainties of the

ambient solar wind speed and solar wind magnetic field. When cross-field diffusion is ignored, an ensemble simulation will still be able to sample different shock locations. One can of course, include cross-field diffusion in the ensemble simulation approach. Assuming that the ambient solar wind upstream of the CME-driven shock can be described by a Parker field, we have run simulations with cross-field diffusion included and the results do not differ much from the ensemble simulation without cross-field diffusion. This is expected since we assume the angular spreading of Earth to be 10° in the ensemble simulation approach, which is similar to that caused by cross-field diffusion (Hu et al. 2017).

Figure 5 shows the evolution of the shock surface as a function of time. The shock locations at eight different times are shown as the black solid curves at $t = 2$ minutes, 12 minutes, 30 minutes, 48 minutes, 70 minutes, 100 minutes, 120 minutes, 160 minutes, respectively. The color in panels a

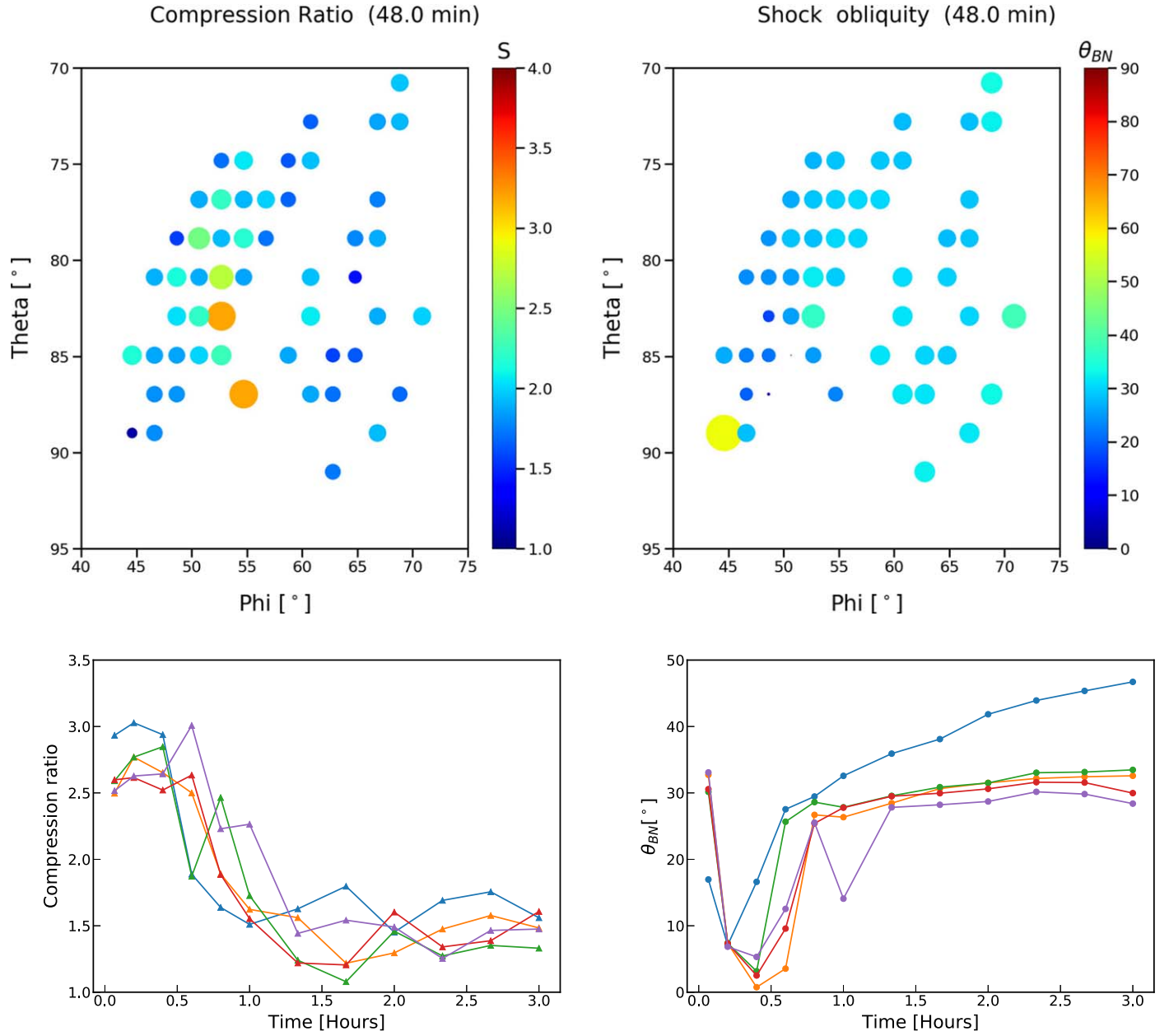


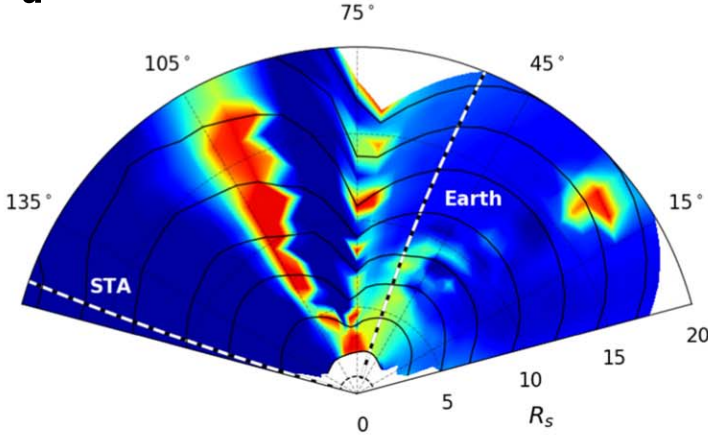
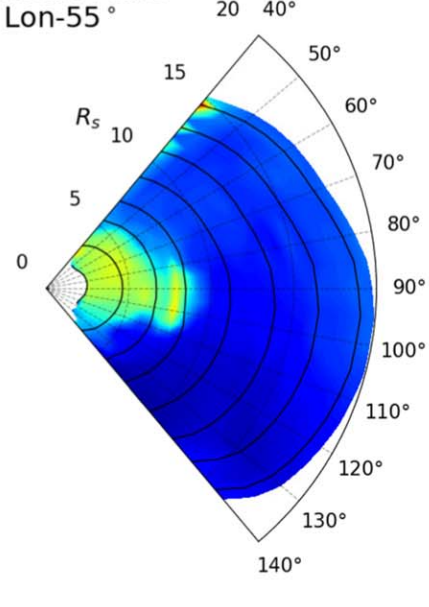
Figure 4. Upper left-hand panel: 65 field lines uniformly chosen in a 10° circle centered at the $L1$ point and tracked back to the shock surface at $t = 48$ minutes along the ambient solar wind magnetic field. Colors on the shock surface represent the compression ratio. Upper right-hand panel: Similar to the left-hand panel but the shock obliquity angles are shown. Theta and Phi are colatitude and longitude in the Heliocentric Earth Ecliptic (HEE) coordinates. Lower left-hand panel: the compression ratio at the shock front for the first 3 hr for five (randomly chosen from the 65 shown above) field lines. Lower right-hand panel: same as the lower left-hand panel, but for the shock obliquity angle θ_{BN} .

and b represents the effective compression ratio s and the shock obliquity θ_{BN} , respectively. The effective compression ratio is calculated as $s = \frac{U_{up} - V_A \cos \theta_{BN}}{U_{dn}}$ where U_{up} and U_{dn} are the upstream and downstream solar wind speed in the shock frame and V_A is the upstream Alfvén speed.

In both panels a and b, the left-hand is the cut on the ecliptic plane and the right-hand is a cut on the Meridian plane containing Earth with $\phi = 55^\circ$. The simulation domain of AWSoM is from 0 to $30 R_s$, 5° to 155° in longitude (the ecliptic plane in the left-hand) and from south 50° to north 50° in latitude (the meridian plane in the right-hand). The shock front was identified along the \hat{r} direction at the place with the largest radial jump of entropy $\Delta s / \Delta r$ at a series of non-equal spacing times. The entropy is evaluated using $s = \ln(T_p / \rho^\gamma)$ where T_p is

the proton temperature and γ is the polytropic index ($\gamma = 5/3$). The angular resolutions of the AWSoM code are 1° in both longitude and latitude. In calculating the shock properties, such as the compression ratio and the shock normal, interpolation of plasma values at the nearest grid points from the identified shock location are used. From Figure 5, we can see that the longitudinal extent of the shock at the innermost location (the first solid curve with $r \sim 2R_s$) is smaller than the simulation domain in both longitudes and latitudes. Indeed, at the first time step, no shock structure is identified between colatitude of 40° – 50° and 120° – 140° (in the HEE coordinate system) in the Meridian plane. In the ecliptic plane, the shock structure at the first time step is approximately a circle. However, starting from the second time step, the shock structure develops a convex

Ecliptic Plane

aMeridian Plane
Lon-55°

Ecliptic Plane

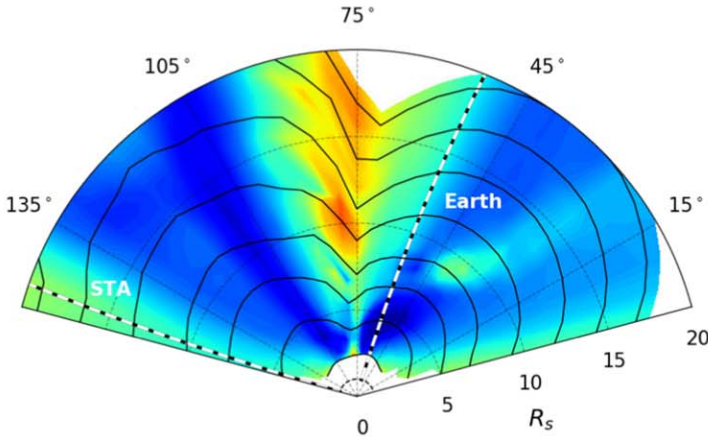
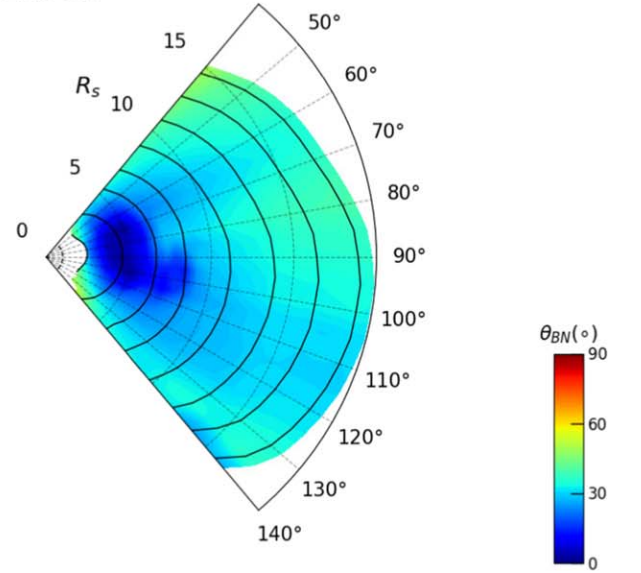
bMeridian Plane
Lon-55°

Figure 5. Upper panel: Early evolution of shock locations and the compression ratio at the shock front in the ecliptic plane (left-hand) and the meridian (right-hand) plane. The radial unit is in solar radius R_s . The white dash curves signal the magnetic field line connected to Earth and STA, respectively. The color shows the compression ratio. Lower panel: same as the upper panel but the color shows the shock obliquity angle θ_{BN} .

shape near $\phi = 70^\circ$. This feature continues and becomes more prominent at the outermost shock location, where a clear “V” shape of the shock surface can be seen. This shock shape is due to the pre-event ambient solar wind and the flux rope that we inserted in the AWSOM model (Jin et al. 2018). In the work of Ding et al. (2020), a similar shape of the shock front was modeled by a double Gaussian injection profile.

Figure 6 shows the shell structures at $t = 120$ minutes in the ecliptic plane (left-hand) and the meridian plane with a longitude of 55° in the HEE coordinate (right-hand). These are the 3D analogs of Figure 3 of Li et al. (2005). The black curves behind the shock (red curve) are the shell boundaries. In

each shell, multiple cells, centered at multiple longitudes and latitudes exist. Similar to the shock front shown in Figure 5, the angular extension of the shells increases with r , both in longitude and latitude. Particles that escape upstream propagate to the observer at 1 au before the shock does. As we discussed in Section 2.2, we use a backward stochastic differential equation method to solve the focused transport equation. In this work, we follow quasi-particles along field lines as shown in the ensembles of Figure 4 until they encounter the shock surface. These particles intersect with the shock at different times. From these locations and times, the energetic particle spectra at the shock are then read off from the iPATH module.

Ecliptic Plane

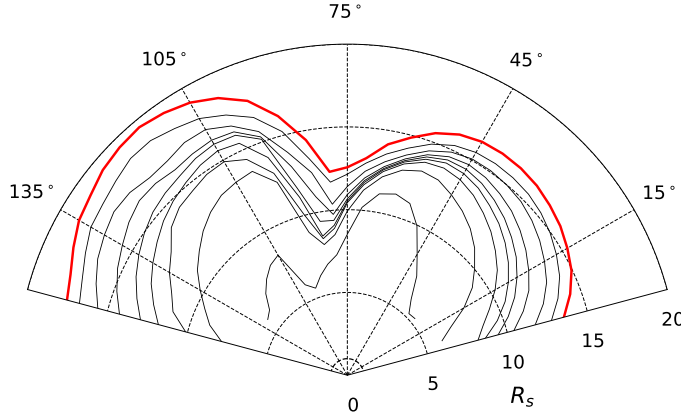
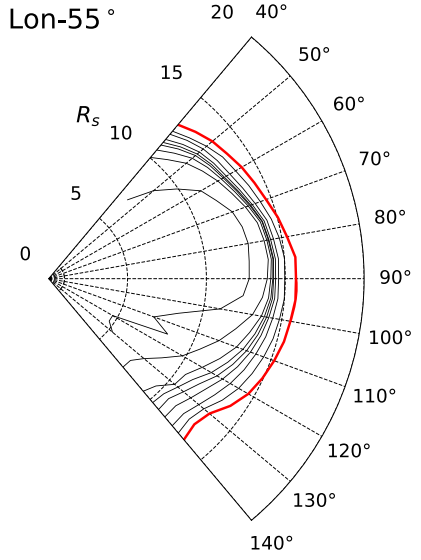
Meridian Plane
Lon-55°

Figure 6. Shell structure behind the shock at $t = 120$ minutes in the ecliptic plane and the meridian plane with a longitude of 55° in the HEE coordinate. The red curves denote the shock front. See text for more details.

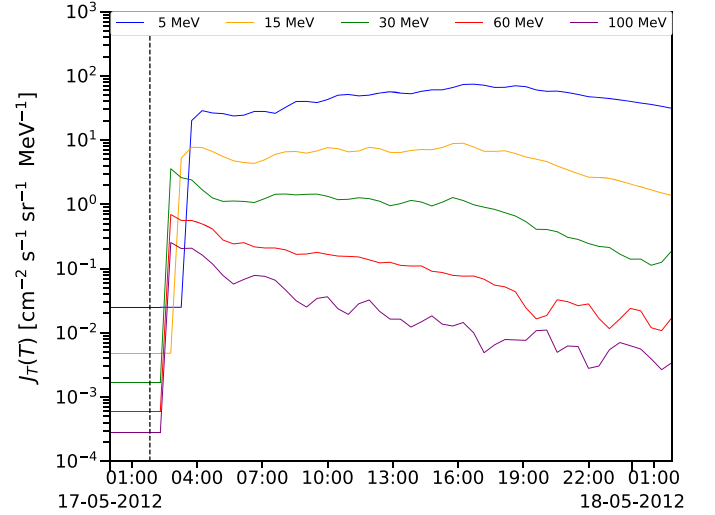
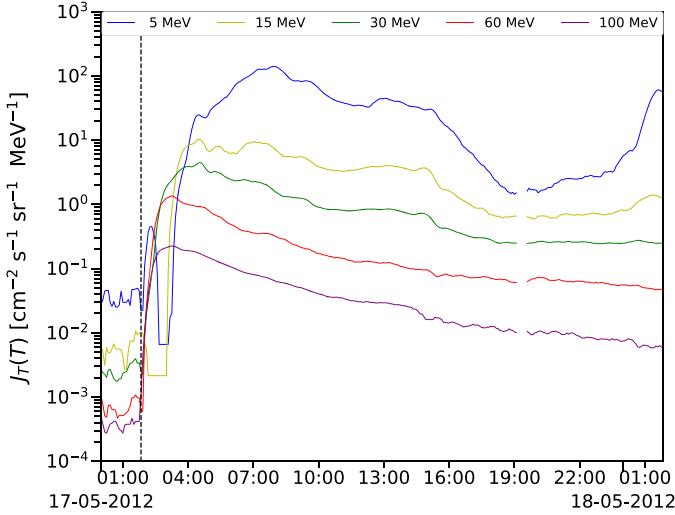


Figure 7. Time intensity profiles for the first 24 hr since the flare eruption from the GOES-15 observation (left-hand panel) and the model calculation (right-hand panel). Five energy bins are shown. From top to bottom, these are 5, 15, 30, 60, and 100 MeV. For better viewing, the profiles are shown two hours prior to the event. The dashed-vertical lines mark the onset of the event.

Figure 7 shows the observed (left-hand) and modeled (right-hand) proton time profiles from 2012-05-17 1:50 to 2012-05-18 1:50. Level 2 data from the westward looking Energetic Proton, Electron, and Alpha Detector (EPEAD) onboard GOES-15 for five energies: 5, 10, 30, 60, and 100 MeV, are shown. These profiles are similar to those shown in Figure 2 of Battarbee et al. (2018), who used GOES-13 data. We only show the time profiles for the first 24 hr because we are mostly interested in the beginning phase of the event. Beyond 24 hr, the time profile generally decays. However, because the shock was not observed in situ at the Earth, there was no clear energetic storm particle (ESP) phase. However, there was a clear drop for $\lesssim 30$ MeV channels around 15:00 UT on 2012-05-18, which possibly indicates that the shock is beyond 1 au after that time. The modeled profile agrees well with the observation. For the highest three energy channels, we can see the characteristic rising phase that is then followed by a gradual decay. Note that the flux is not adjusted freely but is fully decided once the

injection efficiency is determined. For the 5 MeV energy channel, the simulation had a longer gradual rising phase than what was observed, although the peak value is similar.

To further compare observations and simulations, in Figure 8 we show the time integrated particle spectra from 2012-05-17 1:50 to 2012-05-18 1:50, with an 3 hr increment of interval. The ending times are shown at the top of every panel. For comparison, the red curves are the observations by the EPEAD and High Energy Proton and Alpha Detector (HEPAD) instruments onboard GOES-13, based on the Bruno (2017) calibration. There is a very good agreement between the observations and the simulations. The agreements become better over time, in particular for the 24 hr interval (8th panel) when the simulated spectrum is almost on top of the observed one for the entire energy range from 2 MeV to 1 GeV. Note that no scaling parameters are applied to the simulation results. The absolute value of the flux is fully decided by the injection efficiency η (Li et al. 2003, 2005). From our previous

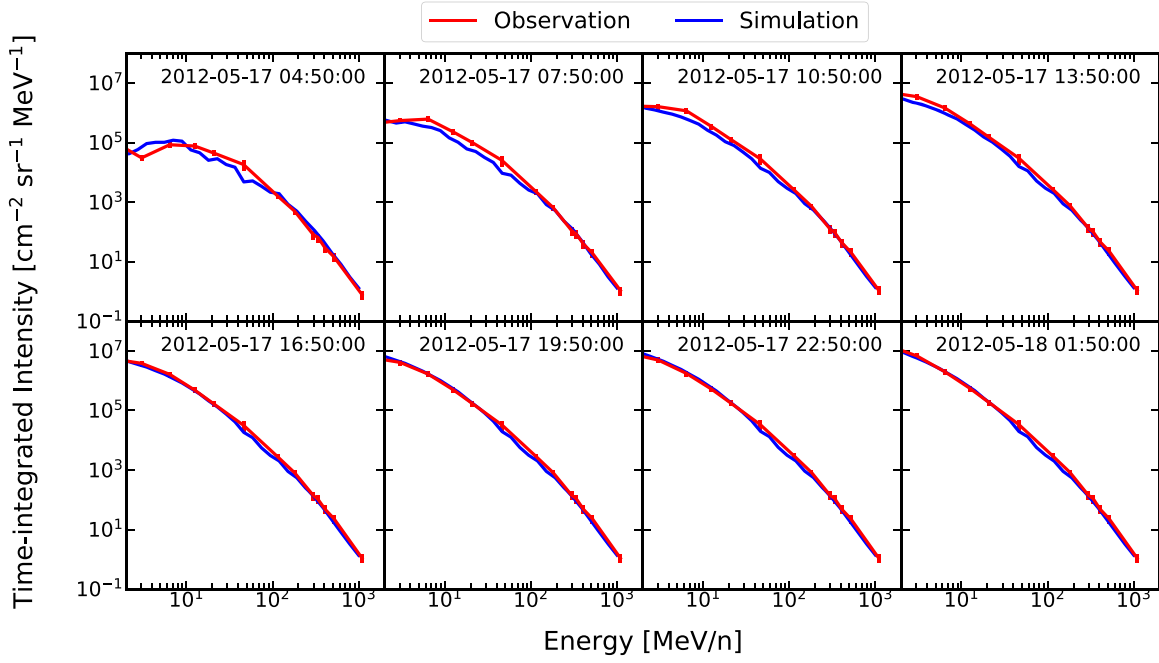


Figure 8. Cumulative proton spectra with a 3 hr interval increase. The starting time for these spectra was 2012-05-17 01:50:00, and the ending times are shown in each individual panel. The GOES observation is in red and the model calculation in blue.

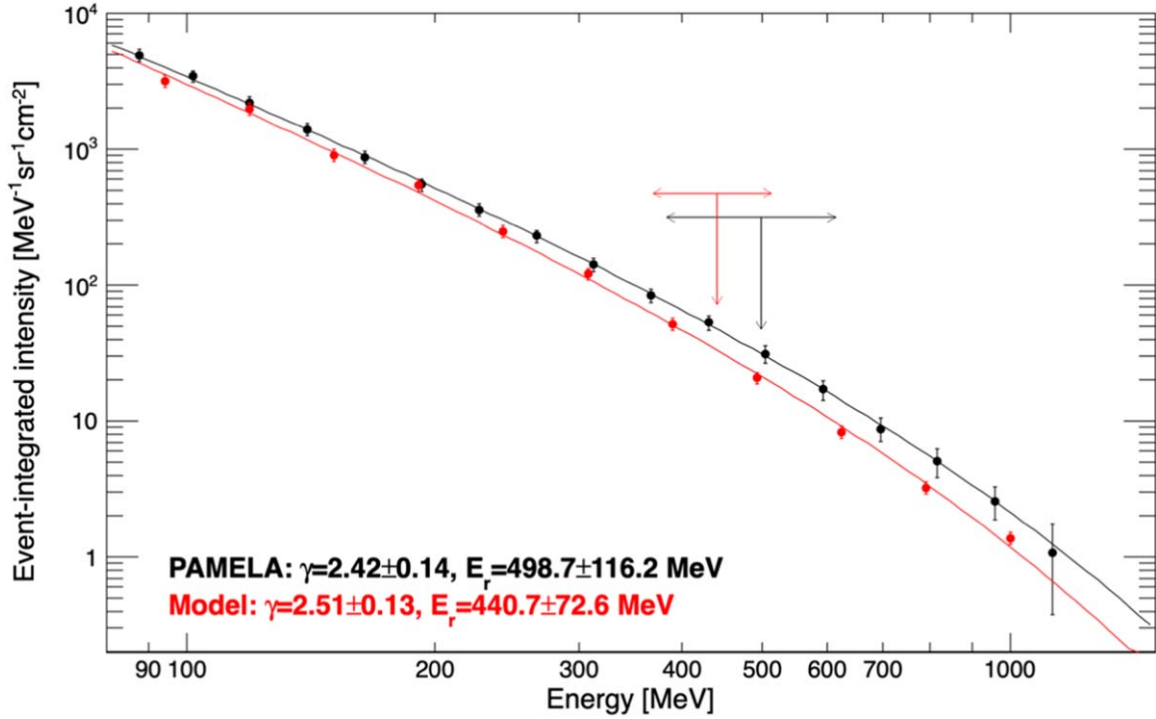


Figure 9. Spectrum comparison between PAMELA observation shown in Bruno et al. (2018, 2019) and our model simulation. The roll-over feature at high energy can be seen in both the observation and the simulation. The fitted parameters correspond to a Ellison–Ramaty spectral fitting. The black and red arrows indicated the location of the roll-over energies with the uncertain indicated by the horizontal bars.

experience of PATH and iPATH modeling (Li et al. 2012b; Hu et al. 2017; Ding et al. 2020), η often ranges between 0.1% to a few percents. Different choices of η determine both the maximum particle energy and the overall energetic particle intensity. In our simulation, we adjust η so that the peak of the modeled 100 MeV proton intensity is close to the measured one in Figure 7. The value of η is found to be 0.002. Once η is fixed, the maximum particle energy cannot be freely adjusted

and the evolution of the time interval spectra is fully decided by the iPATH code. Therefore, the agreement between the interval spectra of the observation and the simulation indicates that the iPATH model captures some of the essential physics of the underlying proton acceleration and transport process in this SEP event.

We now take a closer look at the high-energy end of the spectra. Figure 9 shows a comparison between the event-

integrated spectrum from the PAMELA observation (Bruno et al. 2018, 2019) and the simulation at energies above 80 MeV. The red curve is the model result and the black curve shows the observation from PAMELA (Bruno et al. 2018). The simulation is for the first 24 hr. The period for the PAMELA observation spectrum is from 2012 May 17 01:47 to May 19 10:37, ~ 57 hr. However, the spectrum estimated for the first 24 hour is very similar to the 57 hr event-integrated spectrum due to very small contribution of intensities in the decaying phase. For the simulation, a 15% uncertainty for the intensity is assumed to represent model uncertainty due to (for example) magnetic connection, solar wind speed, magnetic field strength, and so on. This model uncertainty yields a similar value to the observation at ~ 100 MeV. However, the observed intensity is $\sim 10\%$ higher than the simulation at 100 MeV and the difference becomes larger at higher energies, which indicates a less efficient acceleration by the model. However, note that both the maximum energy and the shape of the modeled and the observed spectra are remarkably similar. In particular, both exhibit a high-energy cutoff (or roll-over) that can be attributed to particles escaping from the shock region during acceleration due to the shock's limited extension and lifetime (e.g., Ellison & Ramaty 1985; Lee 2005; Bruno et al. 2018, 2019). Fitting both spectra by the Ellison & Ramaty (1985) functional form

$$\Phi(E) \propto E^{-\gamma} \exp(-E/E_r) \quad (4)$$

yields the spectral indices to be $\gamma = 2.42 \pm 0.14$ for PAMELA observation and $\gamma = 2.51 \pm 0.13$ for the simulation; and the roll-over energy to be $E_r = 498.7 \pm 116.2$ MeV for PAMELA observation and $E_r = 440.7 \pm 72.6$ MeV for the simulation. Using the first 24 hr observation of PAMELA, we obtain similar results. The simulated spectral indices and the break energies agree very well with those observed. In particular, the locations of predicted and measured spectral rollover are consistent within errors, as indicated by the arrows in Figure 9. Note that at these energies, particles are accelerated early in the event when the shock is still below $10 R_s$. Therefore, the usage of the AWSOM code is crucial because it provides shock profiles that are as low as $\sim 2 R_s$.

One notable feature of the iPATH model is its ability to simultaneously obtain the time profiles and particle spectra at multiple locations. Besides Earth, the 2012 May 17 event was also observed by the STA spacecraft and the Radiation instrument onboard the Mars Science Laboratory (Battarbee et al. 2018). The event was also observed by the MESSENGER spacecraft and marginally by STB. At STB, there was only discernible intensity enhancement from the pre-event background for energy channel below 60 MeV. The enhancement of the 25–53 MeV channel is only ~ 10 , which is to be compared to $\sim 2 \times 10^4$ at GOES. In our model simulation, the STB was not connected to the shock and we do not find clear enhancement of protons at STB. Therefore, we do not consider STB in the following. The MESSENGER spacecraft was at a similar longitude as the STA. However, its observational data needs to be carefully processed (Battarbee et al. 2018), so we also do not consider it in this work. The MSL is at ~ 1.46 au, having a similar HGI latitude as the Earth (-7.3° versus -2.4°), and is west to the Earth by 39° . Assuming that the solar wind speed at the MSL and at the Earth are the same, the foot-point of the Parker field passing through the Mars is found to be 12° west to that passing through the Earth. We can therefore model

the time profiles at MSL using the ensemble approach in a similar fashion as that at the Earth. To be specific, we trace back particles from the MSL to the shock surface assuming that particles propagate along an ensemble of 65 field lines which are those field lines as in Figure 4, but shifted along the shock surface by 12° to the west.

We next examine the time profile and event-integrated spectrum at STA. As shown in the left-hand panel of Figure 5(a), STA was to the west of the CME shock and was not magnetically connected to the shock early in the event. Consequently, the intensity profile observed at STA was much lower than that at the Earth. To reach STA, particles accelerated at the shock have to undergo cross-field diffusion. A key parameter in modeling the longitudinal spreading of particles in SEP event is the perpendicular diffusion coefficient κ_\perp . Using the Non-Linear Guiding Center (NLGC) Theory (Shalchi 2010), Hu et al. (2017) and Ding et al. (2020) have adopted a functional form of $\kappa_\perp/\kappa_\parallel \sim v^{\alpha_0} B^{\alpha_1} r^{\alpha_2}$, where v is particle speed, B is solar wind magnetic field, and r is heliocentric distance. In modeling the 2017 September 10 event, Ding et al. (2020) used $\alpha_0 = -2.9$, $\alpha_1 = -2.4$, and $\alpha_2 = -3.8$. We assume the same radial and magnetic field dependence in this work but allow α_0 to vary to fit the STA time intensity profile. The choice of α_0 can affect the relative intensity between low and high-energy protons. We find that a combination of a reference value of $\kappa_\perp/\kappa_\parallel = 0.02$ for 60 MeV proton at 1 au and $\alpha_0 = 7/9$ yields the best fitting result.

Figure 10 shows the time profiles at STA. The left-hand panel is an observation from the High-Energy Telescope (HET) on STA (von Rosenvinge et al. 2008) and the right-hand panel is from simulation. The four energy bands from observations are 13.6–15.1 MeV, 20.8–23.8 MeV, 33.4–35.8 MeV, 60–100 MeV, respectively. The observed shock arrival time at STA was around 12:43 local time on 2012/5/18 and the modeled shock arrival time is 6.5 hr later. The intensity profiles for the two lower energy bins show clear increases after the shock arrival. Presumably, these are particles accelerated at early times but have been kept in the downstream of the shock. The right-hand panel shows the simulation results at 14.3, 22.2, 34.5 and 60 MeV. The simulation agrees reasonably well with the observation. At the two lowest energies, the modeled time profile reaches a peak earlier than the observation by ~ 6 hr. However, the peak intensity between the simulation and observations are close, while the simulated intensities are slightly higher. The modeled intensity profile for the 34.5 MeV proton is very close to the observation throughout the event. The modeled intensity profile for the 60 MeV proton is lower than the observation, smaller by a factor of two for the peak intensity.

Figure 11 shows the proton fluence prior to the shock arrival at STA. Besides data from the HET instrument, data from the Solar Electron and Proton Telescope (SEPT) (Müller-Mellin et al. 2008) and the Low Energy Telescope (LET) (Mewaldt et al. 2008) are also used. The left-hand panel is for observation and the right-hand panel is for simulation. The energy range is from 3 MeV to 100 MeV. The observation is shown as the blue triangles and the simulation as the red squares. As can be seen from the figure, the simulation agrees well with the observation. We note that this agreement depends on the choice of the perpendicular diffusion coefficient (or the ratio of $\kappa_\perp/\kappa_\parallel$), which may differ for different events. We therefore anticipate

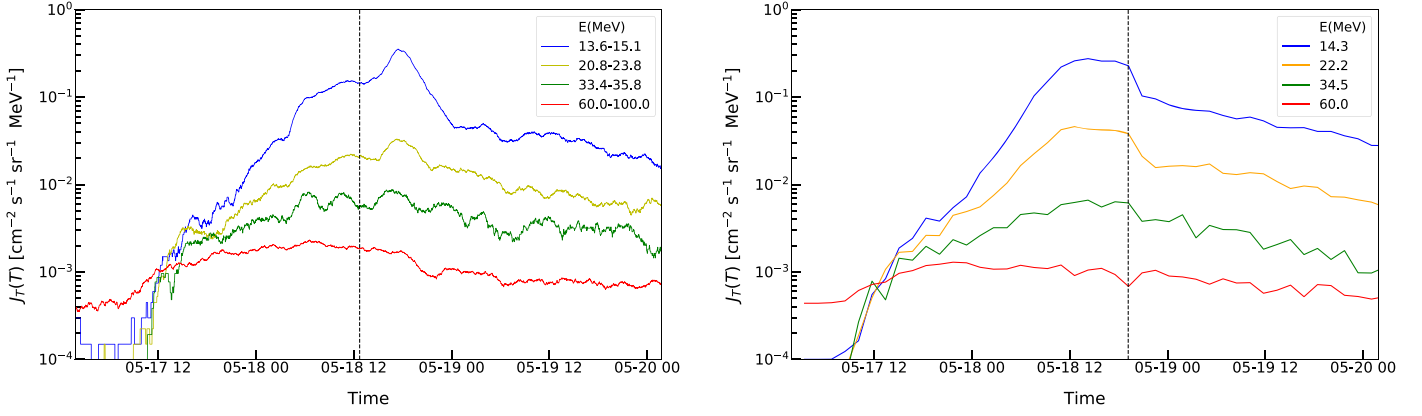


Figure 10. Left-hand panel: time profiles of protons for four energy bins as observed by STEREO-A; right-hand panel: model calculations from AWSOm+iPATH. The vertical-dashed lines mark the shock arrival from observation and the model calculation.

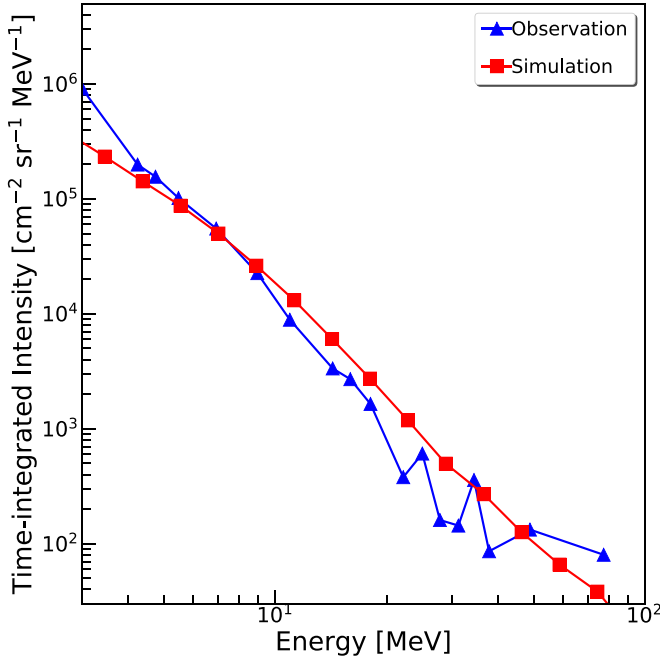


Figure 11. Observed and modeled proton fluence prior to the shock arrival at STA for the 2012 May 17 event. See text for details.

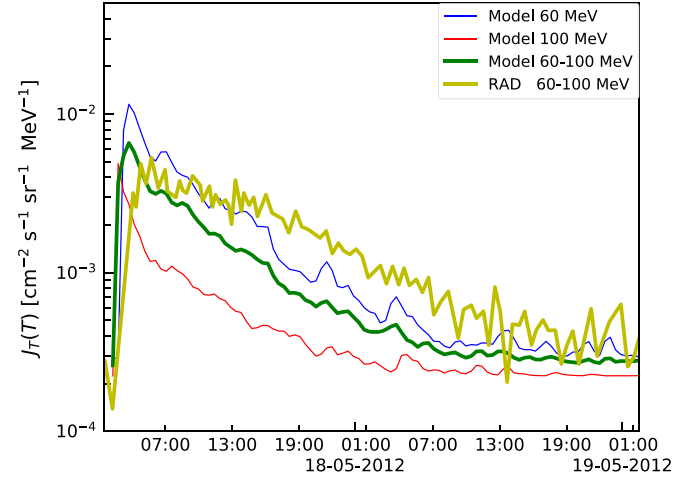


Figure 12. The time profiles of protons from observation and simulation at Mars within 48 hr after eruption. The modeled energy channels of 60 MeV and 100 MeV are shown in thin blue and red curves and the modeled energy bins of 60–100 MeV are shown in thick green. The thick-brown curve is the flux in the energy bin of 60–100 MeV from the RAD instrument on the MSL (adapted from Battarbee et al. 2018).

showed the power of the combined AWSOm+iPATH approach in modeling SEP events at multiple locations.

4. Conclusion

that future studies of different multiple spacecraft events can help us to better understand the nature of κ_{\perp} .

Finally, we consider the 24 hr time profiles of protons as observed by MSL/RAD. Particles from four energy channels: 12–24 MeV, 24–40 MeV, 40–60 MeV, and 60–100 MeV are obtained by MSL/RAD (Hassler et al. 2012). However, as noted by Battarbee et al. (2018), the MSL/RAD data contains both primaries and secondaries due to spacecraft shielding, therefore obtaining accurate counts is challenging. Here we compare our simulation results to the observed flux for the energy bin of 60–100 MeV processes by Battarbee et al. (2018). The observation data is shown as the brown curve in Figure 12. The green curve is its counterpart from the model calculation. The thin blue and the thin red curves are the fluxes at the lower end of the energy interval 60 MeV and at the higher end of the energy interval 100 MeV, respectively. From the figure, we can see that the model predicts a faster rise and a faster decay than the observation, but the peak value is remarkably close to that observed. This comparison, again,

In this paper, we present a model calculation of the 2012 May 17 SEP event by combining the AWSOm and the iPATH models. The AWSOm model is used to describe both the pre-event background solar wind and the CME itself for the first 3 hours when the CME is below $20 R_s$. The CME-driven shock is identified numerically in the AWSOm code and the shock parameters are passed to the iPATH model, from which the accelerated particle spectrum at the shock front is computed. Multiple cells are constructed behind the shock and followed numerically. These shells propagate out with the solar wind and energetic particles convect with shells and diffuse among them. When particles escape upstream the shock, they propagate along the IMF. Using a backward stochastic differential equation method, we follow the propagation of these energetic protons upstream the CME-driven shock in the solar wind. Proton time intensity profiles at five different energies and cumulative particle spectra at eight different times were obtained at L1. These are shown in Figures 7 and 8,

respectively. The simulation results agree nicely with the observations. The iPATH model also allows us to obtain time intensity profiles and particle spectra at different locations. Figures 10 and 11 show the time profiles and fluence of protons at the STA location. Again, good agreements between the model and observations are obtained.

The 1D PATH model has been used to examine individual SEP events with moderate success (Verkhoglyadova et al. 2009, 2010). The characteristics of particles with energy below 100 MeV/nuc are largely captured by the PATH model. However, the PATH model tended to underestimate the maximum particle energies. Very recently, using the iPATH model, which is a 2D extension of the PATH model, Ding et al. (2020) examined the large event on 2017 September 10. They found that to account for the high-energy particles observed at Earth, a double Gaussian profile of the CME-driven shock needed to be invoked. A double Gaussian profile was motivated by white-light observations of CMEs. By introducing this profile, the L1 point was able to be connected to portions of the shock that have a quasi-parallel geometry and a large compression ratio, therefore more efficient particle accelerators, especially when the shock was still close to the Sun. Besides L1 observations, Ding et al. (2020) also obtained reasonable time profiles for energy $\lesssim 200$ MeV protons at the Mars and at the STEREO-A spacecraft. This requires no extra fine-tuning of iPATH because it is an intrinsic 2D code. The work of Ding et al. (2020) suggests that it is crucial to take into account of shock geometry and its evolution during the entire event if we wish to better understand SEP events. The inner boundary of the PATH model is at $20 R_s$ and that of the iPATH model is at $10 R_s$. However, efficient particle acceleration in large SEP events, and in particular GLE events, often occurs very early in the shock evolution and as close as several solar radii to the solar surface. The average shock formation height for GLE events is at $\sim 1.43 R_s$ (Gopalswamy et al. 2017), which provides ample time to accelerate the highest energy particles prior to their release between $2\text{--}5 R_s$ (Reames 2009a, 2009b). Clearly, to examine particle acceleration below $10 R_s$, it is necessary to follow the propagation of a CME and/or the shock that it drives below $10 R_s$. By combining the AWSoM code with the iPATH code, we now capture this critical period of shock evolution and particle acceleration. Using the AWSoM code, which incorporates much of the physics of coronal mass eruption, we obtain a detailed 3D description of the CME-driven shock when it is below $20 R_s$. By feeding this CME shock structures to the iPATH code, we are able to investigate particle acceleration at CME-driven shocks from a few solar radii to $\sim 20 R_s$.

While this work only marks our initial attempt of combining the AWSoM and iPATH, one may already see the power of this approach. The first panel of Figure 8 shows the spectra for the first 3 hr when the shock is still below $20 R_s$ with the shock parameters are obtained from the AWSoM code. There is good agreement between the observed spectrum and that modeled, especially at high energies within these 3 hr, demonstrating the importance of modeling the shock at low altitudes. Furthermore, the correspondence between the high-energy spectral roll-over measured by PAMELA and our model calculation (Figure 9) suggests that both magnetic connection and the evolution of shock parameters at early times are dominant factors contributing to the observed particle spectra at 1 au, and presumably other locations as well. The combined AWSoM

+iPATH model provides an important new tool to investigate spectral features at high energies. In the future, we plan to extend this work to other high-energy SEP events. In particular, we will examine the relationship between the low-energy spectral break and the high-energy spectral roll-overs, which may be produced at different phases of CME propagation. When the shock is beyond $20 R_s$, we use the less computation-demanding iPATH code to follow the CME. As time evolves, we see that the lower energy part of the modeled particle spectra increases with time and comes closer to the observations. This is not surprising because it already emerged in the earlier event modeling using the 1D PATH model (Verkhoglyadova et al. 2009, 2010). The shell structure in PATH and the cell structure in iPATH are unique features of PATH/iPATH. Behind the shock, these cells serve as a moving reservoir of energetic particles. Particles accelerated at the shock front can be confined within these shells (diffusion among them) and be released over an extended period. Apart from a physics-based treatment of the acceleration process at the shock, the cell structures in the iPATH model are likely to be another reason why the iPATH model calculations agree well with observations.

Space Weather study is taking a central role in space plasma research. Understanding large SEP events is essential for future deep space explorations. In this work, we take an initial attempt at combining the state-of-the-art AWSoM code of CME initiation and propagation with the physics-based particle acceleration code of iPATH code to model the 2012 May 17 event. Reasonable results for time intensity profiles and particle spectra are obtained at both Earth and STA locations. Further efforts along this line in modeling other individual events will be reported in the future.

This work is supported in part by NASA grants K99055CT, 80NSSC19K0075, 80NSSC19K0831, and 80NSSC19K0079 at UAH; G.L., M.J., A.B. and G.D. acknowledge support from the NASA/HSR program NNH19ZDA001NHSR. D.L. acknowledges support from NASA/LWS programs NNH17ZDA001N-LWS and NNH19ZDA001N-LWS. The work of B.M.R., G.A.D., A.B., G.L., M.J., and L.M. was also supported, in part, by the Goddard Space Flight Center Internal Scientist Funding Model (competitive work package) program. Supports by ISSI and ISSI-BJ through the international teams 469 is also acknowledged.

ORCID iDs

Gang Li  <https://orcid.org/0000-0003-4695-8866>
 Meng Jin  <https://orcid.org/0000-0002-9672-3873>
 A. Bruno  <https://orcid.org/0000-0001-5191-1662>
 G. A. de Nolfo  <https://orcid.org/0000-0002-3677-074X>
 B. M. Randol  <https://orcid.org/0000-0002-9307-4804>
 J. Ryan  <https://orcid.org/0000-0003-3534-5968>
 D. Lario  <https://orcid.org/0000-0002-3176-8704>

References

- Axford, W., Leer, E., & Skadron, G. 1977, *ICRC*, 11, 132
- Battarbee, M., Guo, J., Dalla, S., et al. 2018, *A&A*, 612, A116
- Bell, A. R. 1978a, *MNRAS*, 182, 147
- Bell, A. R. 1978b, *MNRAS*, 182, 443
- Bian, N. H., & Li, G. 2021, *ApJ*, 908, 45
- Blandford, R. D., & Ostriker, J. P. 1978, *ApJ*, 221, L29
- Borovikov, D., Sokolov, I. V., Roussev, I. I., Taktakishvili, A., & Gombosi, T. I. 2018, *ApJ*, 864, 88

- Bruno, A. 2017, *SpWea*, **15**, 1191
- Bruno, A., Bazilevskaya, G. A., Boezio, M., et al. 2018, *ApJ*, **862**, 97
- Bruno, A., Christian, E., de Nolfo, G., Richardson, I., & Ryan, J. 2019, Proceedings of 29th International Cosmic Ray Conference—PoS (ICRC2019), 358, 1061
- Desai, M. I., Mason, G. M., Dayeh, M. A., et al. 2016, *ApJ*, **828**, 106
- Ding, L.-G., Jiang, Y., & Li, G. 2016, *ApJ*, **818**, 169
- Ding, Z.-Y., Li, G., Hu, J.-X., & Fu, S. 2020, *RAA*, **20**, 145
- Dresing, N., Gómez-Herrero, R., Heber, B., et al. 2014, *A&A*, **567**, A27
- Drury, L. O. 1983, *RPPh*, **46**, 973
- Ellison, D. C., & Ramaty, R. 1984, *AdSpR*, **4**, 137
- Ellison, D. C., & Ramaty, R. 1985, *ApJ*, **298**, 400
- Firoz, K. A., Zhang, Q. M., Gan, W. Q., et al. 2014, *ApJS*, **213**, 24
- Fu, S., Jiang, Y., Airapetian, V., et al. 2019, *ApJ*, **878**, L36
- Gibson, S. E., & Low, B. C. 1998, *ApJ*, **493**, 460
- Gopalswamy, N., Mäkelä, P., Yashiro, S., et al. 2017, *JPhCS*, **900**, 012009
- Gopalswamy, N., Xie, H., Akiyama, S., et al. 2013, *ApJL*, **765**, L30
- Gopalswamy, N., Xie, H., Mäkelä, P., et al. 2013, *AdSpR*, **51**, 1981
- Gordon, B. E., Lee, M. A., Möbius, E., & Trattner, K. J. 1999, *JGR*, **104**, 28263
- Hassler, D. M., Zeitlin, C., Wimmer-Schweingruber, R. F., et al. 2012, *SSRv*, **170**, 503
- Hu, J., Li, G., Ao, X., Zank, G. P., & Verkhoglyadova, O. 2017, *JGRA*, **122**, 10938
- Hu, J., Li, G., Fu, S., Zank, G., & Ao, X. 2018, *ApJL*, **854**, L19
- Jin, M., Manchester, W. B., van der Holst, B., et al. 2017a, *ApJ*, **834**, 172
- Jin, M., Manchester, W. B., van der Holst, B., et al. 2017b, *ApJ*, **834**, 173
- Jin, M., Petrosian, V., Liu, W., et al. 2018, *ApJ*, **867**, 122
- Kozarev, K. A., Evans, R. M., Schwadron, N. A., et al. 2013, *ApJ*, **778**, 43
- Krymskii, G. 1977, *DoSSR*, **234**, 1306
- Lee, M. 1983, *JGRA*, **88**, 6109
- Lee, M. a. 2005, *ApJS*, **158**, 38
- Lee, M. A., & Ryan, J. M. 1986, *ApJ*, **303**, 829
- Li, C., Firoz, K. A., Sun, L. P., & Miroshnichenko, L. I. 2013, *ApJ*, **770**, 34
- Li, G., Moore, R., Mewaldt, R. a., Zhao, L., & Labrador, a. W. 2012a, *SSRv*, **171**, 141
- Li, G., Shalchi, A., Ao, X., Zank, G., & Verkhoglyadova, O. P. 2012b, *AdSpR*, **49**, 1067
- Li, G., Zank, G. P., & Rice, W. K. M. 2003, *JGRA*, **108**, 1
- Li, G., Zank, G. P., & Rice, W. K. M. 2005, *JGRA*, **110**, 1
- Li, G., Zank, G. P., Verkhoglyadova, O., et al. 2009, *ApJ*, **702**, 998
- Linker, J. A., Caplan, R. M., Schwadron, N., et al. 2019, *Journal of Physics: Conference Series*, 1225, 12007
- Manchester, W. B. I., van der Holst, B., Tóth, G., & Gombosi, T. I. 2012, *ApJ*, **756**, 81
- Manchester, W. B. I., Vourlidas, A., Tóth, G., et al. 2008, *ApJ*, **684**, 1448
- Mewaldt, R. A. 2006, *SSRv*, **124**, 303
- Mewaldt, R. A., Cohen, C. M., Cook, W. R., et al. 2008, *SSRv*, **136**, 285
- Mewaldt, R. A., Cohen, C. M. S., Mason, G. M., Haggerty, D. K., & Looper, M. D. 2005, 24th International Cosmic Ray Conference Pune, 1, 101
- Müller-Mellin, R., Böttcher, S., Falenski, J., et al. 2008, *SSRv*, **136**, 363
- Ng, C. K., Reames, D. V., & Tylka, a. J. 2003, *ApJ*, **591**, 461
- Nitta, N. V., Schrijver, C. J., Title, A. M., & Liu, W. 2013, *ApJ*, **776**, 58
- Parker, E. N. 1958, *ApJ*, **128**, 664
- Reames, D. V. 2009a, *ApJ*, **693**, 812
- Reames, D. V. 2009b, *ApJ*, **706**, 844
- Rice, W. K. M., Zank, G. P., & Li, G. 2003, *JGRA*, **108**, 1
- Schwadron, N. A., Townsend, L., Kozarev, K., et al. 2010, *SpWea*, **8**, S00E02
- Shalchi, A. 2010, *ApJ*, **720**, L127
- Shen, C., Li, G., Kong, X., et al. 2013, *ApJ*, **763**, 114
- Sokolov, I. V., van der Holst, B., Oran, R., et al. 2013, *ApJ*, **764**, 23
- Tóth, G., van der Holst, B., & Huang, Z. 2011, *ApJ*, **732**, 102
- Tóth, G., van der Holst, B., Sokolov, I. V., et al. 2012, *JCoPh*, **231**, 870
- van der Holst, B., Manchester, W. B. I., Frazin, R. A., et al. 2010, *ApJ*, **725**, 1373
- van der Holst, B., Sokolov, I. V., Meng, X., et al. 2014, *ApJ*, **782**, 81
- Verkhoglyadova, O. P., Li, G., Zank, G. P., et al. 2010, *JGRA*, **115**, A12103
- Verkhoglyadova, O. P., Li, G., Zank, G. P., Hu, Q., & Mewaldt, R. A. 2009, *ApJ*, **693**, 894
- von Rosenvinge, T. T., Reames, D. V., Baker, R., et al. 2008, *SSRv*, **136**, 391
- Zank, G., Rice, W. K. M., & Wu, C. 2000, *JGR*, **105**, 25079